Almond C/Fe$_x$O$_y$ composite material based on biomass porous carbon structure with high-efficiency microwave absorbing properties

Xiaobo Gong[1], Qianli Liu[2], Wei Zhao[1], Zhaopeng Lu[1], and Tao Zhang[2,*]

[1] *School of Ocean Engineering, Harbin Institute of Technology (Weihai), Weihai 264209, China*
[2] *School of Materials Science and Engineering, Harbin Institute of Technology (Weihai), Weihai 264209, China*

ABSTRACT

As a carrier of stealth technology and electromagnetic protection, microwave absorbing materials have received extensive attention from researchers. Herein, a biomass porous C/Fe$_x$O$_y$ composite was prepared by heat treatment of almond shell layers dipped in different concentrations of iron nitrate solution at 600 °C, 800 °C, and 1000 °C, respectively. The composite material was examined and found to have good microwave absorption properties and multi-loss synergistic effects. When the ferric nitrate concentration is 22.3%, and the heat treatment temperature is 800 °C, the minimum reflection loss can be obtained as − 31.8 dB with a thickness of 2.5 mm. The frequency bandwidth with a reflection loss of less than − 10 dB is 4.80 GHz when the absorber thickness is 2 mm. Therefore, almond wood porous biomass carbon exhibits strong microwave absorbing properties and has great application potential in military and civilian fields.

1 Introduction

In recent years, electromagnetic radiation caused by radar monitoring and electronic communication has seriously affected electronic equipment and human health [1], resulting in the increasing demand of microwave absorption materials. Traditional microwave absorption materials still lack weight, thickness, absorption bandwidth, and strength, which are challenging to meet actual requirements [2]. Thus, there is an urgent need to design and fabricate high-performance electromagnetic wave absorption materials.

Since graphite has been used as a radar-absorbing material to fill the interlayer of aircraft skins, carbon materials have attracted considerable attention due to their strong dielectric loss, lightweight, and stable chemical properties. Subsequently, activated carbon, porous carbon, and carbon fiber have gradually become mainstream carbon-based microwave

---

Xiaobo Gong and Qianli Liu have contributed equally to the article.

Address correspondence to E-mail: taoozhang@126.com

absorption materials. Currently, carbon nanotubes [3–6], graphene [7–9], and their derivatives have been commonly employed [10], and improvements in their density, thickness, and poor microwave absorbing ability have been made. Nonetheless, carbon-based materials' single dielectric loss mechanism limits their capacity for microwave absorption [11–13]. Besides, the preparation methods for carbon nanotubes and graphene are relatively complicated, making the preparation process long and demanding. Ferrite materials are the most mature microwave absorption materials, with outstanding microwave absorption performance and low price, but with low corrosion resistance and high density [14, 15]. Designing materials with the advantages of broad effective bandwidth, low density, thin coating thickness, and excellent microwave absorbing capacity through chemical, physical, or material composite methods are the direction of new microwave absorption materials development in the future [16–21]. Herein, a carbon-based magnetic metal composite was formed by compounding carbon materials and ferrite microwave absorbing materials. This material combines the advantages of the two to optimize the performance of the microwave absorption material.

Biomass carbon is a natural carbon source. The unique microscopic pore structure and large specific surface area enhance the impedance matching performance of electromagnetic waves [22, 23]. Coupled with its advantages of low density and easy availability, it has huge potential for microwave absorbing applications [24, 25]. A variety of biomass carbon has been studied, such as oil palm biomass and biochar [26], apium-derived biochar loaded with $MnFe_2O_4$ [27], bamboo charcoal [28], walnut shell [24], and cedar wood [29]. As a plant product with a huge yield, almonds' green bark, shell, and kernel have been utilized in many fields. However, no research has been conducted on an almond wood shell for microwave absorption. This paper selected almond shells and ferric nitrate as raw materials to prepare C/Fe_xO_y composites. Iron-based and ferrite-type materials were added to the almond shells. Different systems inside the material were connected by bonding through chemical reactions. The absorber exhibited excellent microwave absorbing properties and was created with a simple fabrication method using readily available raw materials.

2 Experiment

2.1 Raw materials

Almond wood shell was obtained from Xinjiang, China. High purity nitrogen was purchased from Longkou East China Gas Co., Ltd. Ferric nitrate was purchased from Tianjin Bodi Chemical Co., Ltd. All chemical reagents were of analytical purity and used without further purification.

2.2 Preparation of samples

The preparation process of the almond C/Fe_xO_y composite material is shown in Fig. 1. The almond shells were stirred in a hot water bath at 90 °C for 30 min and washed twice to remove dust and inorganic salt impurities from the shells. The washed almond shells were added to 30 ml of ferric nitrate solution. The solution was immersed ultrasonically for 1 h and then left to sit for 24 h to ensure sufficient contact between the almond shells with the iron nitrate molecules. After suction filtration, the samples were placed in a blast drying oven at 25 °C and heated to a specific constant temperature T_x in a nitrogen atmosphere tube furnace for 2 h. Finally, the temperature was lowered to obtain composite material samples. When the constant temperature T_x was selected as 800 °C, the samples obtained were denoted S1-800, S2-800, and S3-800. When the mass fraction of ferric nitrate is 22.3 wt%, and the constant temperature T_x was 600 °C and 1000 °C, the samples obtained were denoted S2-600 and S2-1000. When the temperature was higher than 600 °C, the sample was cooled to room temperature in the furnace at a cooling rate of 5 °C/min. Specific heat treatment parameters are presented in Table 1.

2.3 Characterization method

The morphological and elemental analysis of the experimental samples were carried out using a scanning electron microscope by field emission (MERLIN Compact, Zeiss, Germany). Its operating voltage was 20 kV.

An energy-dispersive X-ray spectrometer (EDS) in the SEM environment was used to analyze the components of the sample.

An X-ray diffraction (XRD) analyzer model (DX-2700, Dandong Haoyuan Instrument, China) was

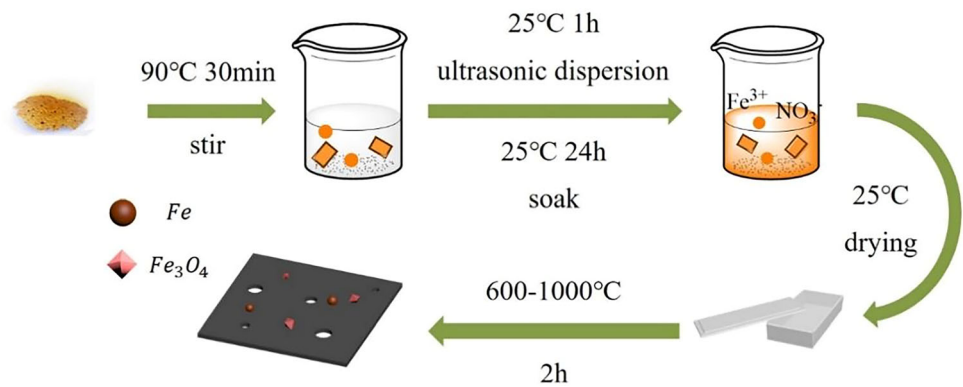**Fig. 1** Preparation process of the C/Fe_xO_y composite material

Table 1 Sample and heat treatment parameters

Sample number	Ferric nitrate solution concentration (wt%)	Preservation temperature (°C)	Heating rate (°C/ min)	Preservation time (h)	Cooling rate (°C/min)
S1-800	0	800	≤ 800 °C: 10	2	≥ 600 °C: 5
S2-600	22.3	600	> 800 °C: 5		< 600 °C: cool in the
S2-800	22.3	800			furnace
S2-1000	22.3	1000			
S3-800	44.6	800			

utilized to identify the structure and phase of the material. The sample was examined with C_u–K_α radiation as the light source under stable conditions. The scanning rate was 4°/min, ranging from 10° to 90°. The acceleration voltage was 30 kV, and the current was 20 mA.

A laser microscope Raman spectrometer (Renishaw inVia, UK) was used to characterize the chemical composition of the sample. The wavelength was 532 nm, and the light intensity was 10%.

Chemical bonds and functional groups of the samples were detected by a Fourier transform infrared spectroscopy (FT-IR) instrument (Nicolet 380, Thermal Electron, USA). The number of scans was 32 times/s. The test range was 400–4000 cm^{-1}, and a transmission mode was used.

The electromagnetic parameters of the samples were examined by a vector network analyzer (N5245A, Agilent, USA). The cable connector that was employed was an Agilent 85050C. The inner diameter was 3 mm, the outer diameter was 7 mm, and the cavity depth was 6.948 mm. The test was performed at room temperature using the calculation method, and the measurement range was 2–18 GHz. The sample was mixed with paraffin at a mass ratio of 1:5 to make an absorbing sample ring. The sample

thickness ranged from 1.0 to 5.5 mm, and the absorbing parameters were measured using the coaxial method. The reflection loss (RL) of the material was given by the following formula [3, 30]:

$$Z_{in} = Z_0 \sqrt{\frac{\mu}{\varepsilon}} \tanh\left(j\frac{2\pi fd}{c}\sqrt{\varepsilon\mu}\right) \qquad (1)$$

$$RL(dB) = 20\lg\left|\frac{Z_{in} - Z_0}{Z_{in} + Z_0}\right| \qquad (2)$$

In the equations, Z_{in} denotes the input impedance of the absorbing material, Z_0 denotes the impedance of free space, ε is the dielectric constant, and μ is the permeability. In addition, f is the frequency of the electromagnetic wave, d is the thickness of the absorber, and c is the velocity of the electromagnetic waves in free space.

3 Results and discussions

3.1 Microstructure analysis

Figure 2 shows SEM pictures of samples immersed in different concentrations of ferric nitrate solution. Figure 2a and b shows S1-800, Fig. 2c and d shows S2-800, and Fig. 2e and f shows S3-800. The images

show obvious grooves appearing on the sample surface after heat treatment. Comparing Fig. 2a, c, and e, it can be seen that the concentration of ferric nitrate has little effect on the diameter of the groove. However, as the iron nitrate solution concentration increases, small spherical substances gradually adhere to the surface, which is presumed to be ferrite or iron particles. This result will be verified with XRD analysis. In Fig. 2e, a very different substance from the shell morphology appears in the sample. The EDS energy spectrum (Fig. 2f) shows that the main element is Fe, with trace amounts of C and O. A high concentration of iron nitrate and uneven surface distribution results in a large amount of Fe element, forming a pure iron or iron solid solution. Comparing Fig. 2b and d, an increase in the ferric nitrate solution concentration significantly intensifies the etching degree of the shell surface. The resulting spherical particles tend to appear round, but do not occupy the inside of the micropores.

Figure 3 shows SEM photographs of samples S2-600, S2-800, and S2-1000 obtained by heat treatment at different temperatures. Comparing Fig. 3a, c, and e, the surface of sample S2-600 still has a partially enclosed area, while sample S2-800 appears all grooved with some rectangular grooves. This morphology is similar to another study on biomass carbon, which may be responsible for its improved microwave absorption performance [29]. At a higher temperature, the shell surface of sample S2-1000 tends to be flatter, the groove depth decreases, and the average shell thickness is reduced. In addition, it can be seen that the degree of etching on the shell surface intensified when the heat treatment temperature was increased. The surface defects make it easier for the ferrite particles to be uniformly distributed in the defects rather than clustered together,

Fig. 2 SEM images and EDS spectrum of almond wood C/Fe$_x$O$_y$ composites prepared from different concentrations of ferric nitrate solutions. a and b S1-800, c and d S2-800, e and f S3-800
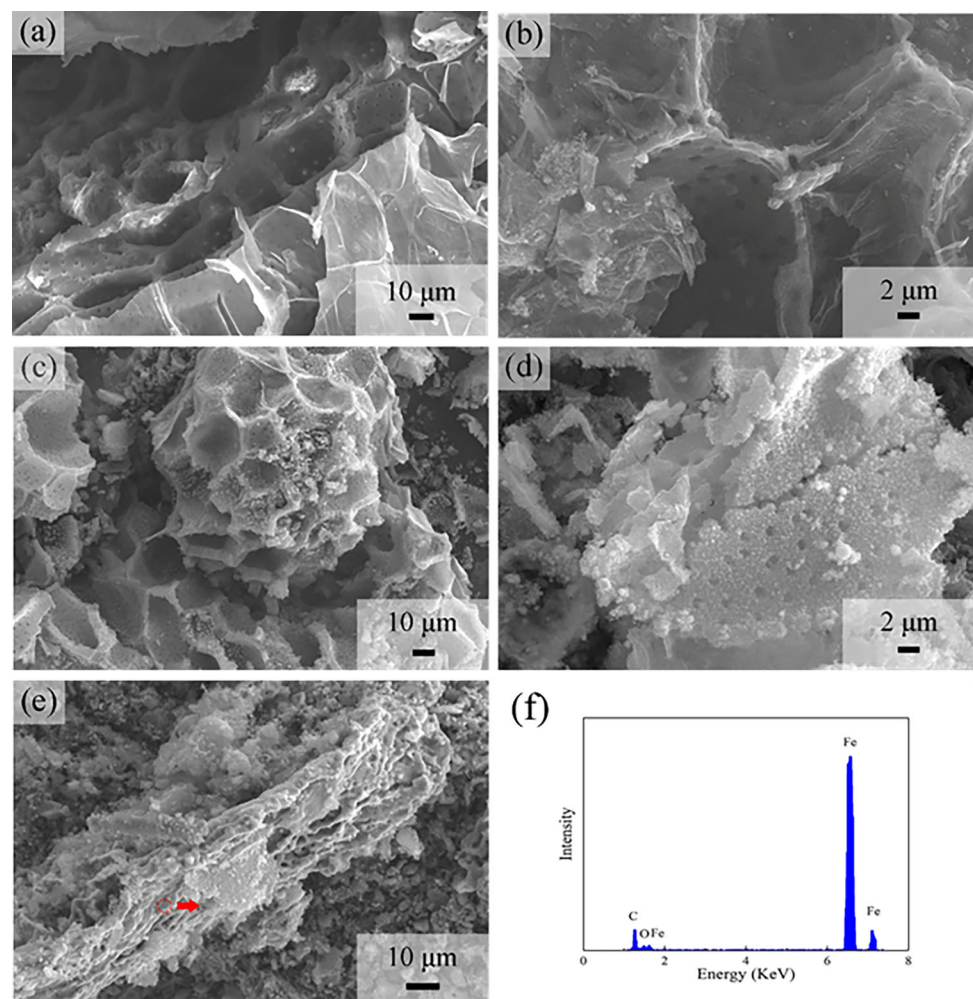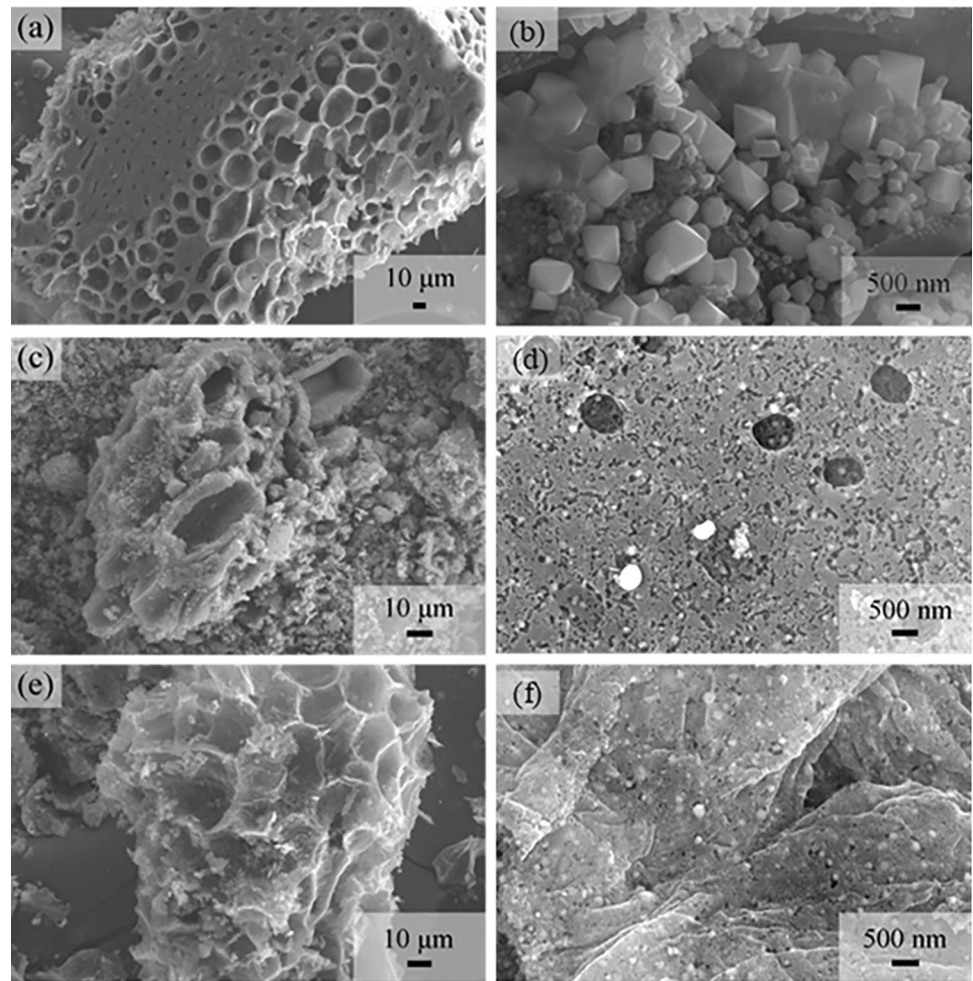
Fig. 3 SEM photographs of samples of almond wood C/Fe$_x$O$_y$ composites with different heat treatment temperatures, **a** and **b** S2-600, **c** and **d** S2-800, **e** and **f** S2-1000

and the defects may also improve the dielectric properties of the material.

Figure 3b, d, and f shows SEM pictures of the micro-area of particles attached to the surface of S2-600, S2-800, and S2-1000. By comparison, it was found that when the heat treatment temperature is 600 °C, the particles attached to the shell surface are octagonal pyramids. A large number of particles are distributed in the recessed part of the groove with particle sizes of 0.1–1.2 μm. According to previous studies [2, 25], these particles could be Fe$_3$O$_4$. The particles turn into an ellipsoid shape at the heat treatment temperature of 800 °C, with a particle size of 0.1–0.8 μm, indicating that most of the ferroferric oxide has been transformed into Fe particles. When the heat treatment temperature is 1000 °C, the particles are almost spherical, ranging from 0.1 to 1 μm. The morphology and composition characteristics of the above particles will be further confirmed by XRD.

3.2 Chemical composition analysis

Figure 4a shows the XRD patterns of C/Fe$_x$O$_y$ composites obtained by heat treatment at different temperatures. It can be seen that S2-600 has a prominent dispersion peak at $2\theta = 23.1°$, which is a typical amorphous carbon peak. In S2-800 and S2-1000, this peak is not evident or even disappears. Instead, there are peaks with smaller intensity at $2\theta = 26.2°$ and 43.9°. These two peaks can be classified as graphitized carbon (JCPDS No. 75-1621, JCPDS No. 75-0623). It indicates that the graphitization degree improves significantly with increasing temperature. In S2-600, the diffraction peaks at $2\theta = 35.4°$, 30.1°, 56.9°, and 62.5° can be classified as the (311), (220), (511), and (440) planes of Fe$_3$O$_4$ (JCPDS No. 99-0073). The intensity of these diffraction peaks is significantly reduced at the corresponding positions of S2-800 and S2-1000, but there is still a trace amount of Fe$_3$O$_4$ (JCPDS No. 88-0866). When the temperature
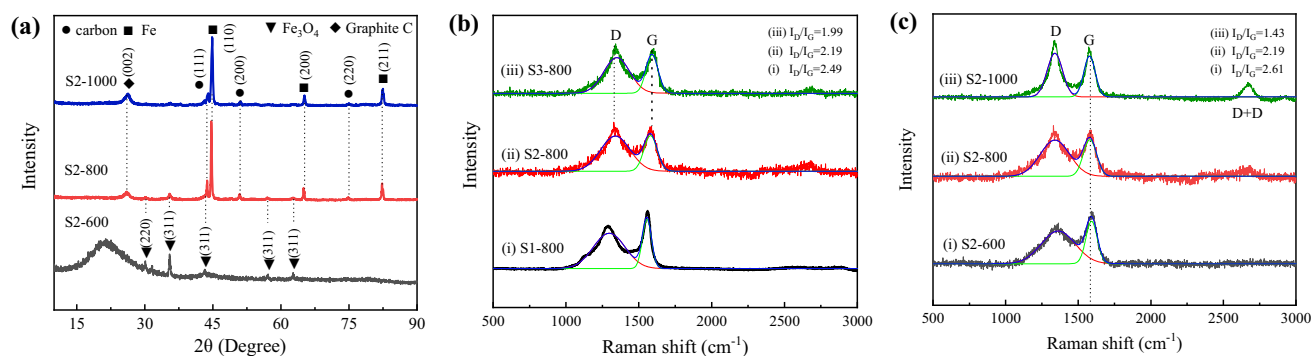
Fig. 4 Analysis of the chemical composition of the almond C/Fe$_x$O$_y$ composite. **a** XRD patterns of composite samples obtained at different heat treatment temperatures; **b** Raman spectra of the C/Fe$_x$O$_y$ composite material (heat treatment temperature: 800 °C) obtained after immersion in different concentrations of ferric nitrate solution; **c** Raman spectra of the C/Fe$_x$O$_y$ composite material (immersed in 22.3 wt% ferric nitrate solution) after different heat treatment temperatures

exceeds 800 °C, the diffraction peaks of the sample at $2\theta = 44.7°$, 65.0°, and 82.3° can be categorized as the (110), (200), and (211) plane of Fe (JCPDS No. 87-0721). The calibration of these diffraction peaks confirms the speculation of the octagonal pyramid Fe$_3$O$_4$ and small spherical Fe particles in the previous SEM pictures.

The Raman spectra of C/Fe$_x$O$_y$ composites prepared under different ferric nitrate concentrations and heat treatment temperatures are shown in Fig. 4b and c, respectively.

The D band in the carbon material is related to the lattice distortion caused by the sp^3 hybridization, reflecting the lattice defects of the material. The G band is assigned to the in-plane stretching vibration of the sp^2 hybridization of C atoms [31, 32]. The D+D band can be used to compare the position and relative intensity of the G band to illustrate the quality and number of graphene layers [33, 34]. The I_D/I_G value is known to be useful to reflect the density of material defects. Samples S1-800, S2-800, and S3-800 have D and G characteristic peaks at approximately 1285 cm^{-1} and 1579 cm^{-1}, respectively. Samples S2-600, S2-800, and S2-1000 have D and G characteristic peaks at 1338 cm^{-1} and 1580 cm^{-1}, respectively. Moreover, two peaks at 2666 cm^{-1} (band D+D) and 2920 cm^{-1} (band D+G) were observed in S2-1000, consistent with the SEM speculation and the findings of graphitized carbon in XRD. By calculating the peak area ratio, the I_D/I_G value gradually decreases from 2.49 to 1.99 as the ferric nitrate solution concentration increases. The I_D/I_G value also gradually falls from 2.61 to 1.43 when the heat treatment temperature increases. This phenomenon may involve multiple

factors. Ferric nitrate will destroy the original C network structure of the biocarbon shell, increase the surface defects of the material, and theoretically increase the I_D/I_G value. However, the uneven distribution of iron nitrate makes it easy for it to aggregate to form a stable structure of Fe at high temperatures, which will reduce the disorder of the material. This finding is consistent with another report mentioning that the precipitation and decomposition of ferrite particles may cause the I_D/I_G value to decrease [35, 36]. Besides, an increase in temperature also intensifies the degree of graphitization, which also lowers the I_D/I_G value.

Incorporating activated carbon into the metal oxide helps form an amorphous metal–carbon structure. The carbon structure can degrade the material's magnetic properties and avoid the formation of unstable bonds on the surface. At high temperatures, carbon reduces iron nitrate to form a mixture of iron oxide, ferroferric oxide, and iron. After reaching a specific temperature, activated carbon reacts with iron or ferrite to form stable chemical bonds O–C–Fe_{1-x}–O [43]. The schematic diagram of mechanism prediction is depicted in Fig. 5. The iron-containing substances and gas products obtained by the reaction at a temperature exceeding 500 °C are presented in Table 2.

The iron-containing substances and gas products obtained by the reaction at a temperature exceeding 500 °C are presented in Table 2.
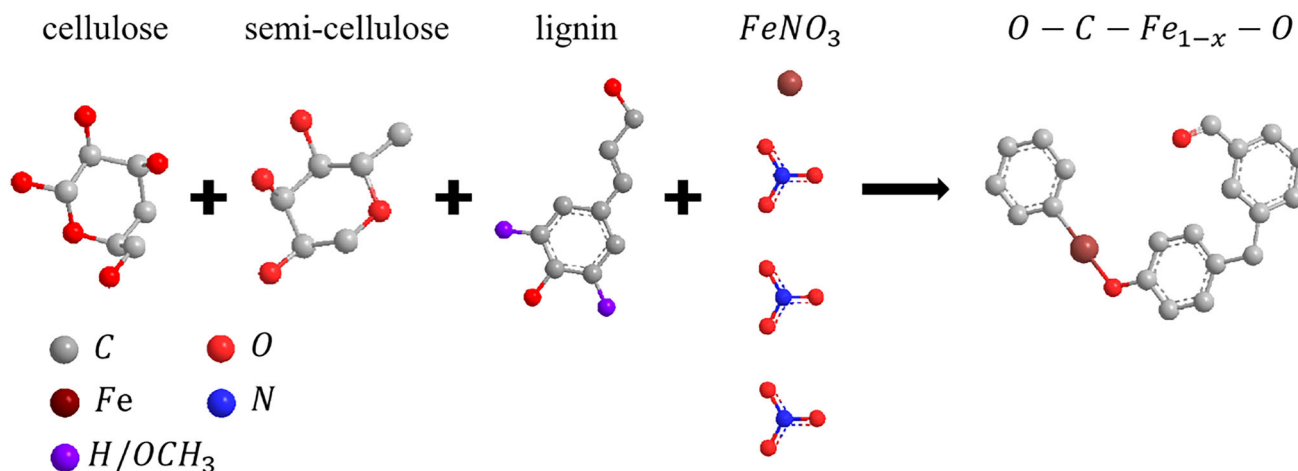
cellulose   semi-cellulose   lignin $FeNO_3$ $O-C-Fe_{1-x}-O$

○ C ● O
● Fe ● N
● H/OCH_3

Fig. 5 The prediction diagram of the mechanism of high-temperature reduction of ferric nitrate in almond shell

Table 2 Iron-containing substances obtained by the reaction

Temperature range (°C)	Solid residue	Gas product
500–600	$Fe(NO_3)_3$, Fe_2O_3, Fe_3O_4	CO, H_2O, CH_4
600–800	Fe_2O_3, Fe_3O_4, Fe	CO_2
800–1000	Fe	CO_2

3.3 Analysis of microwave absorption performance of C/Fe_xO_y

Figure 6 shows the reflection loss curve and impedance matching diagram of the C/Fe_xO_y composite material immersed in different concentrations of ferric nitrate solution and heat treated at 800 °C. It can be seen that, as the concentration increases, the microwave absorbing performance of the material first increases and then decreases. In the S2-800 group, the sample can reach the lowest reflection loss of -31.8 dB at 10.32 GHz when the corresponding thickness is 2.5 mm. The effective frequency bandwidth (RL ≤ -10 dB) is 4.80 GHz (from 11.28 to 16.08 GHz) when the absorber thickness is 2 mm. $Z_{in}/Z_0 = 1$ is a condition for ideal impedance matching where the electromagnetic wave completely enters the internal material for loss or transmission instead of surface reflection. A small amount of iron element increases the conductance loss, which increases the absorbing effect. Excessive iron element makes the impedance matching imbalance and the absorbing effect worse due to the skin effect. From the impedance matching curve, as the concentration of the ferric nitrate solution increases, the impedance matching is first superior and then inferior, which is the same as the reflection loss curve.

Figure 7 shows the electromagnetic parameter diagram of C/Fe_xO_y composites immersed in different concentrations of ferric nitrate solution when heat treated at 800 °C. Figure 7a–c exhibits the dielectric properties of the material, and Fig. 7d–f shows the magnetic properties of the material. In Fig. 7b, the imaginary part of dielectric loss ε'' of the material decreases after a certain concentration of iron nitrate is reduced to ferrite, but ε'' increases after too much ferrite is produced. This phenomenon may be attributed to the uneven distribution of iron nitrate, which leads to the appearance of regular Fe crystal lattices in the shell depressions. The Fe crystal lattices affect the regularity of the C lattices, resulting in higher ε''. In addition, as the concentration of iron nitrate increases, more ferrite is reduced to the elemental iron, which increases the electrical conductivity, and increases the resistance loss and further increases the imaginary part of the dielectric constant. Unlike the dielectric loss imaginary part ε'', the magnetic loss imaginary part μ'' does not vary much from sample to sample. With the increase in iron nitrate concentration, the mean value of the S2 sample is greater than the other two in general, indicating that more ferric nitrate can improve the magnetic loss of the material. In Fig. 7c and f, too much ferric nitrate causes an increase of the dielectric loss
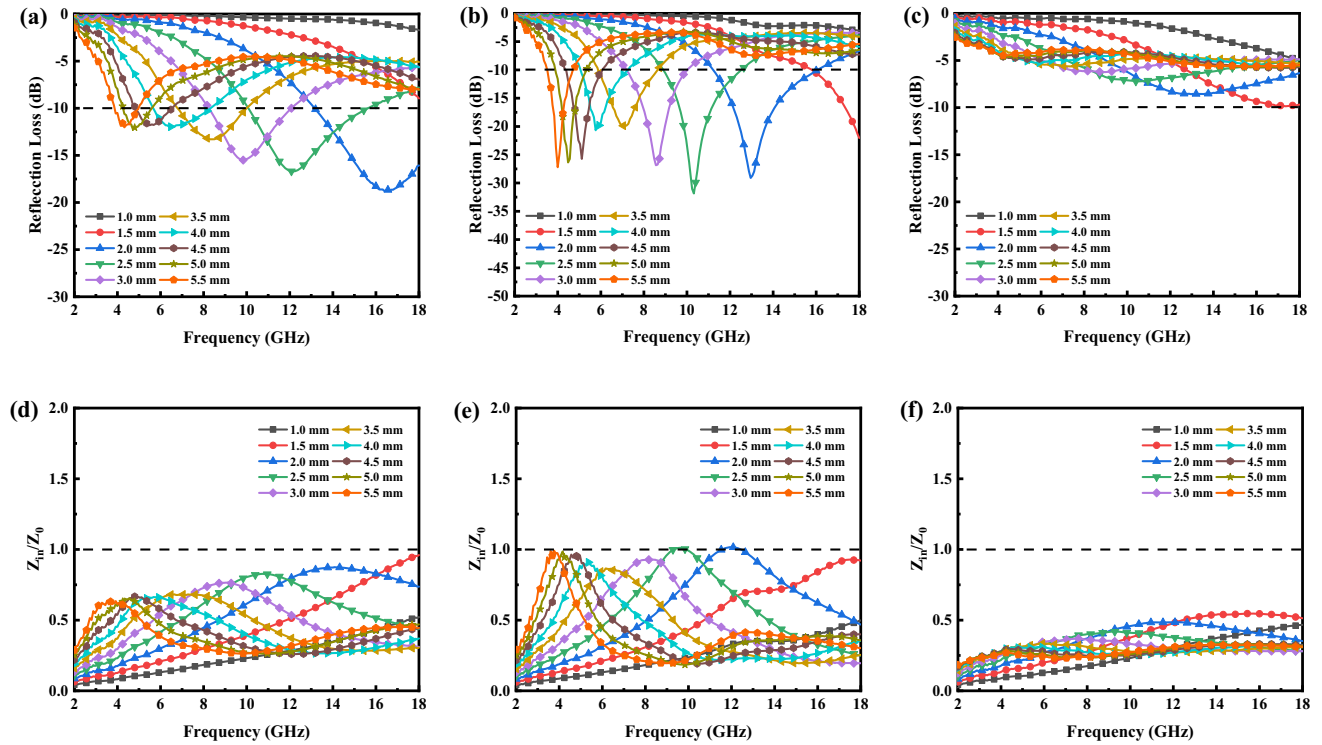
Fig. 6 Reflection loss curve and impedance matching diagram of the C/Fe$_x$O$_y$ composite material (heat treatment temperature: 800 °C) immersed in different concentrations of ferric nitrate solution, **a** and **d** S1-800, **b** and **e** S2-800, **c** and **f** S3-800
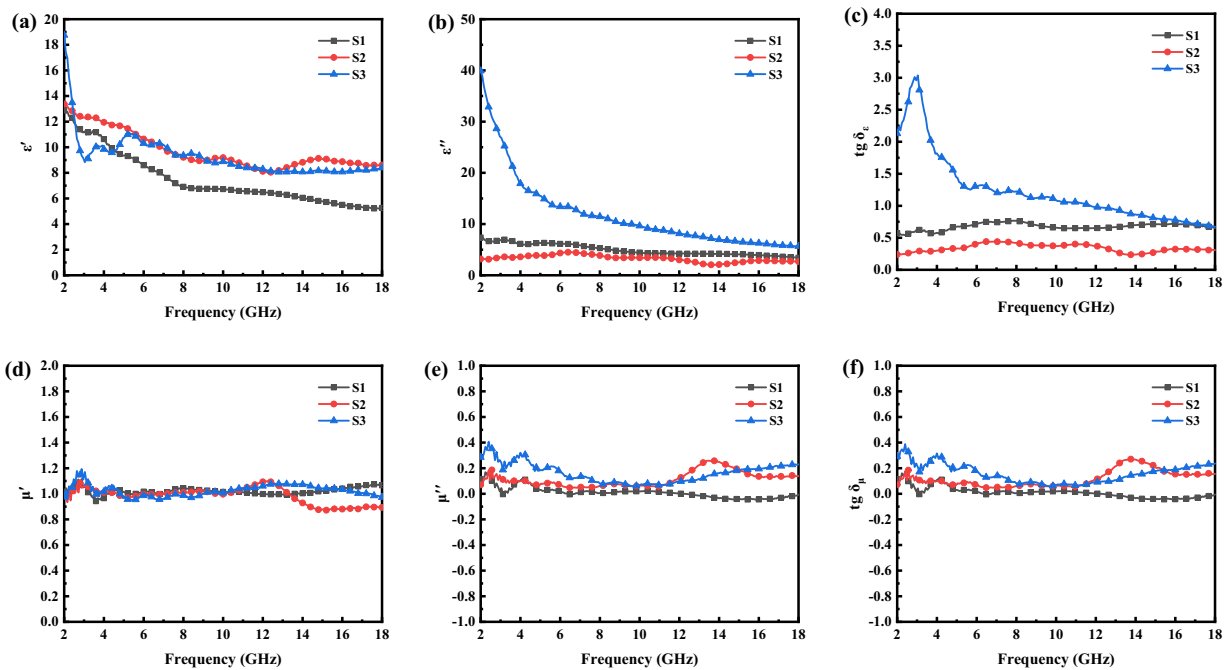

Fig. 7 Electromagnetic parameters of the C/Fe$_x$O$_y$ composite material (heat treatment temperature: 800 °C) immersed in different concentrations of ferric nitrate solution, **a–c** Real part and imaginary part of dielectric constant, the tangent of loss angle, **d–f** Real part and imaginary part of permeability, the tangent of loss angle

tangent, and the gap between the tangent of dielectric loss and the magnetic loss becomes too large, making the impedance matching worse. To summarize, the increase in the concentration of ferric nitrate solution is not proportional to the effect on ε'' and μ''. A certain amount of ferrite will reduce ε'' and increase μ'', making the impedance matching of the material better. However, too much ferrite makes ε'' too high, which ultimately deteriorates the impedance matching performance.

Figure 8 shows the reflection loss curve and impedance matching diagram of the C/Fe$_x$O$_y$ composite immersed in a 22.3 wt% ferric nitrate solution with different heat treatment temperatures. In the S2-600 group, when the absorber thickness is 2.0 mm, the lowest reflection loss (RL) is − 37.9 dB (18 GHz). When the corresponding thickness is 2.5 mm, the effective bandwidth (RL lower than − 10 dB) is 6.64 GHz (11.28–17.92 GHz). The S2-1000 group obtains the widest absorption bandwidth of 7.04 GHz (10.24–17.28 GHz) at 2.5 mm. In S2-800, the lowest reflection loss is only − 31.8 dB at a thickness of 2.5 mm (worse than S2-600), and when the corresponding thickness is 2 mm, the effective absorption bandwidth is 4.80 GHz (narrower than S2-600 and

S2-1000). However, the RL in all thickness groups in S2-800 is below − 20 dB, which can be seen more clearly from the relationship between the reflection loss, frequency, and thickness of S2-800 and S2-600 (Fig. 9), demonstrating that S2-800 exhibits better microwave absorbing properties. Under the influence of temperature, the material shows a dynamic change, with good wave absorption at lower temperatures and worse at higher temperatures. The possible reasons are a decrease in compactness of the shell, an increase in the groove depth, and a transformation of the morphology into the shape of rectangular or similar rectangular with smaller arc. These factors help reduce the reflection of electromagnetic waves and create conditions for the rectangular waveguide to absorb microwaves. Meanwhile, the addition of ferroferric oxide and iron particles improves the microwave absorption performance. However, when the heat treatment temperature reaches 1000 °C, the porous structure of the material is destroyed, and the topography of the shell develops toward planarization, which causes the electromagnetic waves to be easily reflected vertically. The ferroferric oxide disappears completely at excessively high temperatures and turns into iron pellets, and the
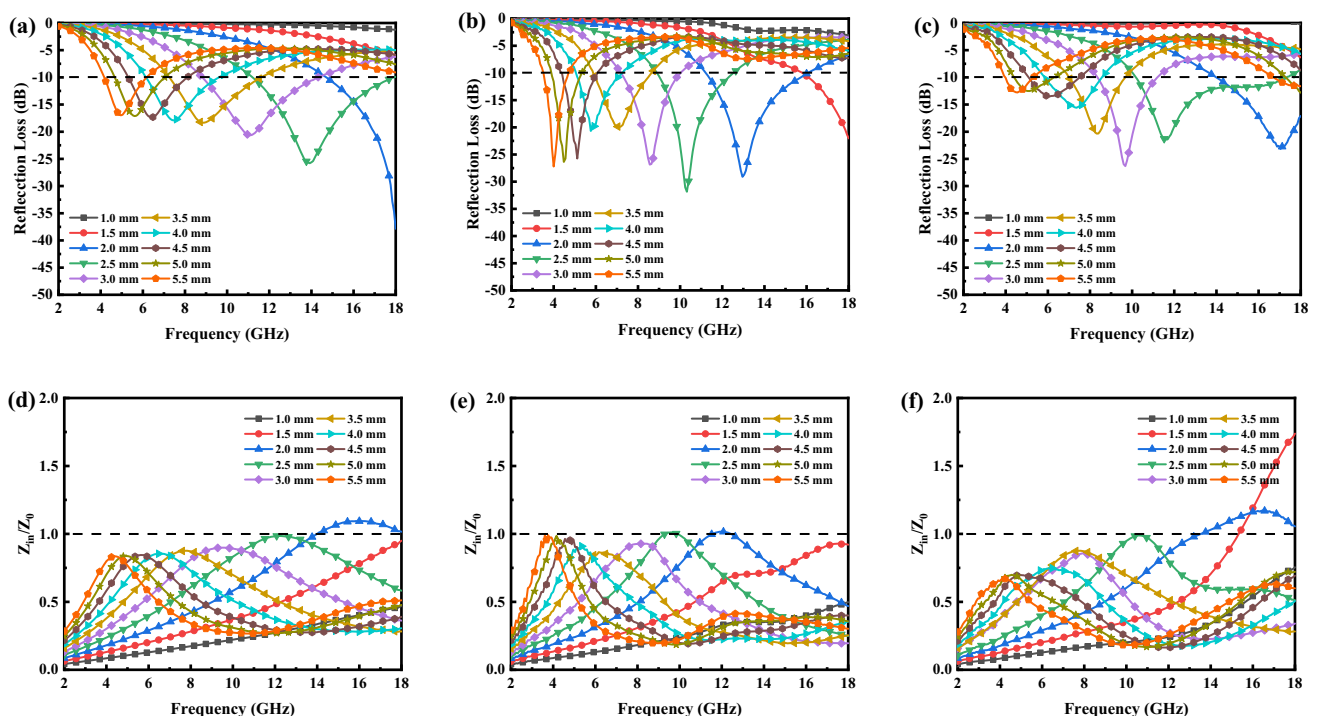

Fig. 8 Reflection loss curve and impedance matching diagram of the C/Fe$_x$O$_y$ composite material (immersed in 22.3 wt% ferric nitrate solution) after being heat treated at different temperatures, **a** and **d** S2-600, **b** and **e** S2-800, **c** and **f** S2-1000
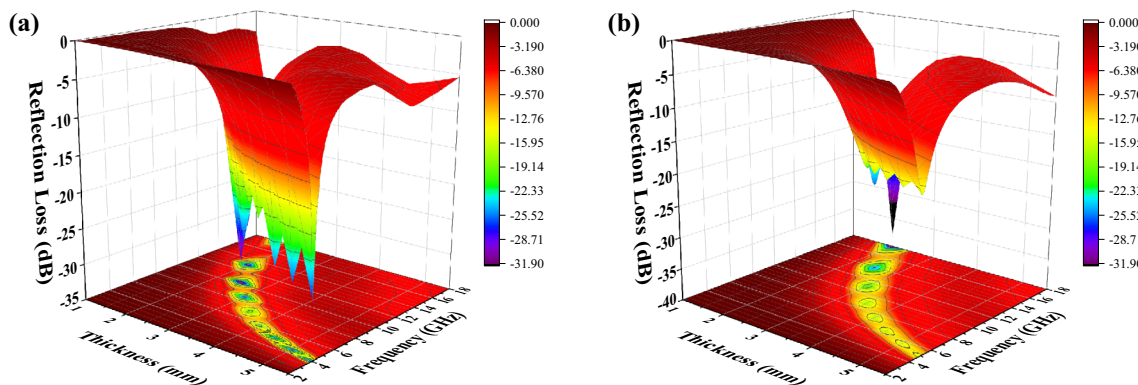
Fig. 9 3D color mapping surface image of the relationship between reflection loss, frequency, and thickness in the C/Fe_xO_y composite material, **a** S2-800, **b** S2-600

absorption performance of pure iron is worse than that of ferric oxide. Moreover, iron aggregation is prone to produce ordered iron crystals, which destroys the impedance matching. Therefore, when the heat treatment temperature is 600 °C or 1000 °C, only part of the thickness of the sample can meet the impedance matching condition, while most samples cannot satisfy $Z_{in}/Z_0 = 1$.

Table 3 below illustrates some typical microwave absorbing materials and their microwave absorbing performance. A closer inspection of the table shows that the C/Fe_xO_y sample prepared in this paper has good absorbing properties, among which the absorbing bandwidth, 7.04 GHz, is excellent. The unique microscopic pore structure and large specific surface area of almonds enhance the impedance matching performance of electromagnetic waves. The appropriate amount of ferric nitrate can effectively improve the electromagnetic wave reflection loss of the material. Almond porous biomass carbon-based

C/Fe_xO_y composite can be an attractive candidate material for microwave absorbers.

To reflect the effect of adding magnetic particles on the polarization and relaxation of the material, Fig. 10a and b shows the Cole diagrams of S1-800 and S2-800. In the Cole diagram, the semi-circular arcs consisting of the experimental points represent a Debye relaxation model [37]. Compared to the number of semi-circular arcs in both samples, it can be seen that there are more semi-circular arcs as the iron nitrate is reduced to ferroferric oxide and iron pellets. From Fig. 10a and b, the trend of the Cole diagram curve in S1-800 is linear, while the semi-circular arc in S2-800 is mostly distorted. In other words, the introduction of magnetic particles increases the degree of distortion of the semi-circular arc, indicating numerous types of electromagnetic loss in S2-800, such as conductance loss and interface polarization. At the same time, the absorption mechanism of a single almond shell carbon-based material is only a resistive-loss mechanism. After adding magnetic

Table 3 Comparison of typical microwave absorbing materials

Materials	Thickness (mm)	RLmax (dB)	Absorption bandwidth (GHz)	References
CNTs/Co-900	1.81	− 60.4	5.2 (12.8–18)	[4]
CR-G/PEO	2.0	− 38.8	5.6 (12.4–18)	[7]
Fe-Co/NPC	1.2	− 21.7	5.6 (12.2–18)	[16]
$CNTs/Co_xFe_{3-x}O_4$	1.18	− 61.86	4.08 ($\sim$ 8–12.08)	[18]
$Co_xFe_{3-x}O_4/MoS_2$	1.57	− 66.38	4.0 ($\sim$ 14.2–18)	[19]
NiCo@C/ZnO	2.3	− 60.97	6.08 ($\sim$ 12–18)	[20]
$MnFe_2O_4$@C	2.5	− 48.92	1.4 (0.38–1.78)	[27]
PBPC-680	4.28	− 68.3	6.13 (8.2–14.33)	[29]
Fe_3O_4@NPC	3.0	− 65.5	4.0 (8–12)	[35]
$PG-Fe_3O_4$	2.7	− 53.0	5.4 (12.6–18)	[36]
C/Fe_xO_y	2.0	− 37.9	7.04 (10.24–17.28)	This work

Fig. 10 Cole diagram of the C/Fe_xO_y composite material heat treated at 800 °C, **a** S1-800, **b** S2-800
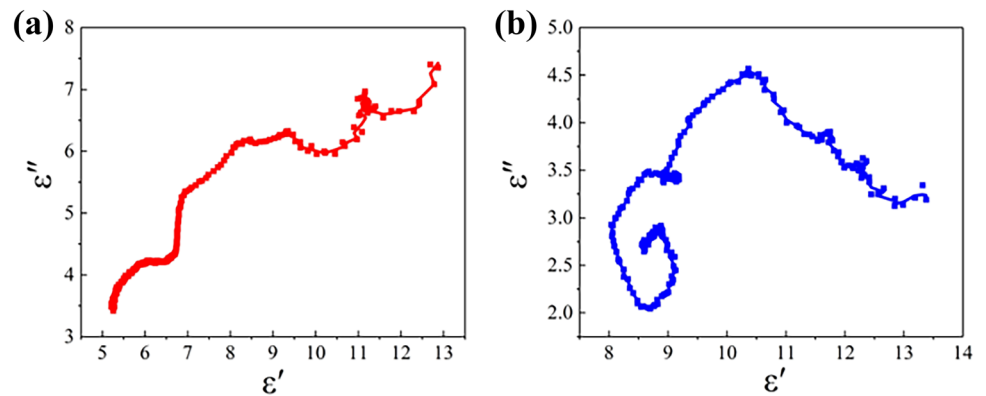
particles, the surface etching of the material increases, and the interface performance improves. As a result, other relaxation behaviors become more active, improving microwave absorption performance and reducing reflection loss [38].

According to the above characterization results, the absorption principle of C/Fe_xO_y composite materials is summarized in Fig. 11. Figure 11a describes the mechanism of action between electromagnetic waves and absorbing rings. A small part of the incident electromagnetic wave is reflected and scattered on the absorber surface, and most are attenuated inside the ring. The remaining electromagnetic wave is transmitted through the ring. The prepared C/Fe_xO_y

composite material has a large number of pores, multilayer interfaces, and a certain amount of magnetic particles. Therefore, there are multiple loss mechanisms for the absorption of incident electromagnetic waves. Figure 11b shows a schematic diagram of electromagnetic wave attenuation and conversion of the C/Fe_xO_y composite material. First, the almond wood biochar shell has a porous, groove-like thin layer microstructure. The lamellar structure means that the material will generate an induced current under an alternating magnetic field and exhibit a resistive-loss mechanism so that part of the electromagnetic wave is dissipated in the form of heat energy. Since the curvature of the groove of the

Fig. 11 Schematic diagram of the microwave absorbing mechanism of C/Fe_xO_y composite materials, **a** loss model of the absorber, **b** multiple loss mechanisms, **c** schematic diagram of polarization caused by functional groups
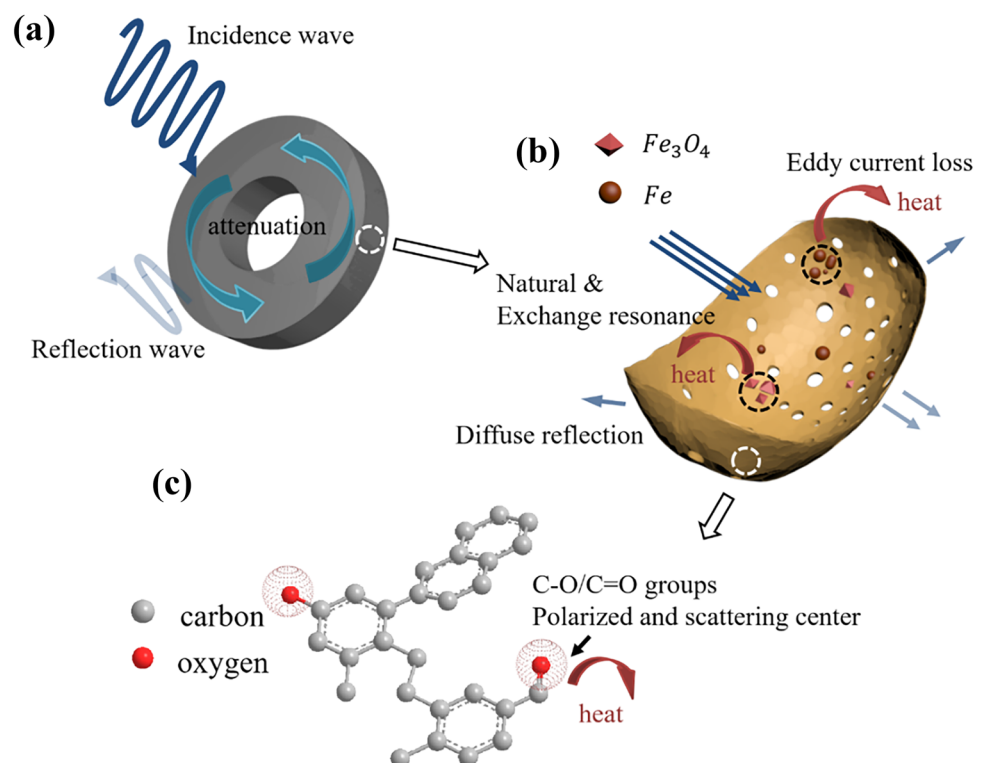
C/Fe_xO_y composite material reaches a maximum under 800 °C heat treatment, this structure reduces the area where the electromagnetic wave incident angle is 0° or close to 0°, effectively curbing the vertical reflection. Secondly, according to the Maxwell Garnett (MG) theory, the numerous porous structures effectively reduce the dielectric constant, improve the resistivity of the carbon matrix, and promote impedance matching [39, 40]. Therefore, the porous and groove-like thin layer structure of the C/Fe_xO_y composite material can increase the transmission path of the electromagnetic waves inside the material and cause multiple reflections, multiple scattering, and Rayleigh scattering. A longer transmission path is beneficial to increase the diffuse reflection loss and significantly reduce the reflection of the material. Moreover, the ferroferric oxide and iron particles produced by reducing iron nitrate can greatly improve the magnetic loss capability, including hysteresis loss, eddy current loss, and residual loss. At 600–800 °C, Fe_3O_4 is in the shape of an octagonal pyramid. The electromagnetic wave loss is mainly through natural resonance and exchange resonance, which is residual loss. Due to the unevenness of the surface of the material, the iron pellets tend to accumulate in the gullies of the shell groove at 800 °C and above. In these iron accumulation areas, small eddy currents can be formed on the surface of the iron particles, which can attenuate electromagnetic waves through eddy current loss or hysteresis loss under the action of an alternating magnetic field [35, 41].

Figure 11c shows the influence of the chemical composition of the C/Fe_xO_y composite material on electromagnetic wave loss. At 600 °C, the material's ether bond and ketone bond are not entirely broken, and the aromatization reaction is not entirely finished. Hence, the C–O and C=O functional groups act as the polarization and scattering center, making the C–C bond polarized, leading to a polarization relaxation phenomenon inside the material, and the loss mechanism appears as dielectric loss [42]. Since polar bonds are broken at higher temperatures, dielectric loss will gradually disappear as the heat treatment temperature increases.

4 Conclusion

In this paper, the almond wood shell and ferric nitrate were selected as raw materials to prepare C/Fe_xO_y composite materials with easy availability and simple preparation methods. This material exhibits excellent microwave absorbing performance, and the multiple loss synergistic effect of ferrite can effectively enhance its function. The effects of ferric nitrate and the maximum heat treatment temperature on the microwave absorbing properties of the composite are analyzed and studied. The appropriate amount of ferric nitrate can effectively improve the electromagnetic wave reflection loss of the material. Excessive addition deteriorates the impedance matching characteristics of the material and reduces the electromagnetic wave reflection loss. Similarly, the increase of temperature improves and then deteriorates the absorption performance of the material. When the concentration of ferric nitrate is 22.3%, and the heat treatment temperature is 800 °C, the minimum reflection loss is − 31.8 dB, and the maximum effective absorption bandwidth is 4.80 GHz. When the heat treatment temperature is 600 °C or 1000 °C, the minimum reflection loss is − 37.9 dB, and the maximum effective absorption bandwidth is 7.04 GHz. Therefore, porous biomass carbon can be an attractive candidate material for lightweight microwave absorber.

Author contributions

XG and QL conceptualized and designed the research, and wrote the paper. WZ and ZL were involved in the data collection and analysis. TZ supervised the project.

Data availability

All data generated or analyzed during this study are included in this published article.

Declarations

Conflict of interest There are no conflict of interest to declare.

References

1. Y.Y. Lu, Y.T. Wang, H.L. Li et al., MOF-derived porous Co/C nanocomposites with excellent electromagnetic wave absorption properties. ACS Appl. Mater. Interfaces **7**(24), 13604 (2015)

2. H. Sun, R.C. Che, X. You et al., Cross-stacking aligned carbon-nanotube films to tune microwave absorption frequencies and increase absorption intensities. Adv. Mater. **26**(48), 8120 (2014)

3. L.N. Wang, X.L. Jia, Y.F. Li et al., Synthesis and microwave absorption property of flexible magnetic film based on graphene oxide/carbon nanotubes and Fe_3O_4 nanoparticles. J. Mater. Chem. A **2**(36), 14940 (2014)

4. Y.C. Yin, X.F. Liu, X.J. Wei et al., Magnetically aligned Co-C/MWCNTs composite derived from MWCNT-interconnected zeolitic imidazolate frameworks for a lightweight and highly efficient electromagnetic wave absorber. ACS Appl. Mater. Interfaces. **9**(36), 30850 (2017)

5. Y.C. Yin, X.F. Liu, X.J. Wei et al., Porous CNTs/Co composite derived from zeolitic imidazolate framework: a lightweight, ultrathin, and highly efficient electromagnetic wave absorber. ACS Appl. Mater. Interfaces **8**(50), 34686 (2016)

6. T. Hou, Z. Jia, Y. Dong et al., Layered 3D structure derived from MXene/magnetic carbon nanotubes for ultra-broadband electromagnetic wave absorption. Chem. Eng. J. **431**, 133919 (2022)

7. X. Bai, Y.H. Zhai, Y. Zhang, Green approach to prepare graphene-based composites with high microwave absorption capacity. J. Phys. Chem. C **115**(23), 11673 (2011)

8. P.B. Liu, Y. Huang, J. Yan et al., Magnetic graphene@PANI@porous TiO_2 ternary composites for high-performance electromagnetic wave absorption. J. Mater. Chem. C **4**(26), 6362 (2016)

9. B. Qu, C.L. Zhu, C.Y. Li et al., Coupling Hollow Fe_3O_4-Fe nanoparticles with graphene sheets for high-performance electromagnetic wave absorbing material. ACS Appl. Mater. Interfaces. **8**(6), 3730 (2016)

10. D. Micheli, C. Apollo, R. Pastore et al., X-Band microwave characterization of carbon-based nanocomposite material, absorption capability comparison and RAS design simulation. Compos. Sci. Technol. **70**(2), 400 (2010)

11. C. Wang, X.J. Han, P. Xu et al., The electromagnetic property of chemically reduced graphene oxide and its application as microwave absorbing material. Appl. Phys. Lett. **98**(7), 072906 (2011)

12. C. Sun, Z. Jia, S. Xu et al., Synergistic regulation of dielectric-magnetic dual-loss and triple heterointerface polarization via magnetic MXene for high-performance electromagnetic wave absorption. J. Mater. Sci. Technol. **113**, 128 (2022)

13. M. Qin, L. Zhang, H. Wu, Dielectric loss mechanism in electromagnetic wave absorbing materials. Adv. Sci. **2022**, 2105553 (2022)

14. S.S. Kim, S.B. Jo, K.I. Gueon et al., Complex permeability and permittivity and microwave-absorption of Ferrite-Rubber composite in X-band frequencies. IEEE Trans. Magn. **27**(6), 5462 (1991)

15. W.M. Zhu, L. Wang, R. Zhao et al., Electromagnetic and microwave-absorbing properties of magnetic nickel ferrite nanocrystals. Nanoscale **3**(7), 2862 (2011)

16. X.M. Zhang, G.B. Ji, W. Liu et al., Thermal conversion of an Fe_3O_4@metal-organic framework: a new method for an efficient Fe-Co/nanoporous carbon microwave absorbing material. Nanoscale **7**(30), 12932 (2015)

17. Y. Zhang, Y. Huang, T.F. Zhang et al., Broadband and tunable high-performance microwave absorption of an ultralight and highly compressible graphene foam. Adv. Mater. **27**(12), 2049 (2015)

18. M. Wu, A.K. Darboe, X. Qi et al., Optimization, selective and efficient production of $CNTs/Co_{(x)}Fe_{(3-x)}O_{(4)}$ core/shell nanocomposites as outstanding microwave absorbers. J. Mater. Chem. C **8**(34), 11936 (2020)

19. L. Long, E. Yang, X. Qi et al., Positive and reverse core/shell structure $Co_xFe_{3-x}O_4/MoS_2$ and $MoS_2/Co_xFe_{3-x}O_4$ nanocomposites: selective production and outstanding electromagnetic absorption comprehensive performance. ACS Sustain. Chem. Eng. **8**(1), 613 (2020)

20. J. Wang, Z. Jia, X. Liu et al., Construction of 1D heterostructure NiCo@C/ZnO nanorod with enhanced microwave absorption. Nano Micro Lett. **13**(1), 1 (2021)

21. C. Li, Z. Li, X. Qi et al., A generalizable strategy for constructing ultralight three-dimensional hierarchical network heterostructure as high-efficient microwave absorber. J. Colloid Interface Sci. **605**, 13 (2022)

22. Z.C. Wu, K. Tian, T. Huang et al., Hierarchically porous carbons derived from biomasses with excellent microwave absorption performance. ACS Appl. Mater. Interfaces. **10**(13), 11108 (2018)

23. J. Zhang, Z. Li, X. Qi et al., Constructing flower-like core@shell $MoSe_2$-based nanocomposites as a novel and

high-efficient microwave absorber. Compos. B **222**, 109067 (2021)

24. X. Qiu, L.X. Wang, H.L. Zhu et al., Lightweight and efficient microwave absorbing materials based on walnut shell-derived nano-porous carbon. Nanoscale **9**(22), 7408 (2017)

25. H.Q. Zhao, Y. Cheng, H.L. Lv et al., A novel hierarchically porous magnetic carbon derived from biomass for strong lightweight microwave absorption. Carbon **142**, 245 (2019)

26. A.A. Salema, Y.K. Yeow, K. Ishaque et al., Dielectric properties and microwave heating of oil palm biomass and biochar. Ind. Crops Prod. **50**, 366 (2013)

27. P.F. Yin, L.M. Zhang, P. Sun et al., Apium-derived biochar loaded with $MnFe_2O_4@C$ for excellent low frequency electromagnetic wave absorption. Ceram. Int. **46**(9), 13641 (2020)

28. K.H. Wu, T.H. Ting, C.I. Liu et al., Electromagnetic and microwave absorbing properties of $Ni_{0.5}Zn_{0.5}Fe_2O_4$/bamboo charcoal core-shell nanocomposites. Compos. Sci. Technol. **68**(1), 132 (2008)

29. J.B. Xi, E.Z. Zhou, Y.J. Liu et al., Wood-based straightway channel structure for high performance microwave absorption. Carbon **124**, 492 (2017)

30. C.R. Paul, *Introduction to Electromagnetic Compatibility* (Wiley-Interscience, Hoboken, 2006)

31. L. Ci, L. Song, C.H. Jin et al., Atomic layers of hybridized boron nitride and graphene domains. Nat. Mater. **9**(5), 430 (2010)

32. M.A. Pimenta, G. Dresselhaus, M.S. Dresselhaus et al., Studying disorder in graphite-based systems by Raman spectroscopy. Phys. Chem. Chem. Phys. **9**(11), 1276 (2007)

33. A. Reina, X.T. Jia, J. Ho et al., Large area, few-layer graphene films on arbitrary substrates by chemical vapor deposition. Nano Lett. **9**(1), 30 (2009)

34. X.S. Li, W.W. Cai, J.H. An et al., Large-area synthesis of high-quality and uniform graphene films on copper foils. Science **324**(5932), 1312 (2009)

35. Z. Xiang, Y.M. Song, J. Xiong et al., Enhanced electromagnetic wave absorption of nanoporous Fe_3O_4 @ carbon composites derived from metal-organic frameworks. Carbon **142**, 20 (2019)

36. Y.W. Zheng, X.X. Wang, S. Wei et al., Fabrication of porous graphene-Fe_3O_4 hybrid composites with outstanding microwave absorption performance. Compos. A **95**, 237 (2017)

37. P.Q. Mantas, Dielectric response of materials: extension to the Debye model. J. Eur. Ceram. Soc. **19**(12), 2079 (1999)

38. X.H. Meng, J. Zhang, L. Xiong et al., In-situ growth of Fe/Fe_3O_4/C hierarchical architectures with wide-band electromagnetic wave absorption. Ceram. Int. **44**(17), 21933 (2018)

39. T. Zhang, J. Zhang, H. Luo et al., Facile approach to fabricate $BCN/Fe_{-x}(B/C/N)_{(y)}$ nano-architectures with enhanced electromagnetic wave absorption. Nanotechnology **29**(23), 235701 (2018)

40. H.Q. Zhao, Y. Cheng, W. Liu et al., Biomass-derived porous carbon-based nanostructures for microwave absorption. Nano-Micro Lett. **11**(1), 1 (2019)

41. R. Meng, T. Zhang, P.Z. Jiao et al., Facile fabrication of SiC/Fe_xO_y embellished graphite layers with enhanced electromagnetic wave absorption. J. Alloy. Compd. **798**, 386 (2019)

42. C. Wang, V. Murugadoss, J. Kong et al., Overview of carbon nanostructures and nanocomposites for electromagnetic wave shielding. Carbon **140**, 696 (2018)

43. D. Tahir, S. Ilyas, B. Abdullah et al., Electronic properties of composite iron (II, III) oxide (Fe3O4) carbonaceous absorber materials by electron spectroscopy. J. Electron Spectrosc. Relat. Phenom. **229**, 47–51 (2018)